

# The large-scale anomalous microwave emission revisited by *WMAP* <sup>★</sup>

G. Lagache<sup>1</sup>

IAS, Bât. 121, Université Paris-Sud, 91435 Orsay, France

Received 24-03-03; Accepted 08-04-03

**Abstract.** We present a new study of the high latitude galactic contributions to the millimeter sky, based on an analysis of the *WMAP* data combined with several templates of dust emission (*DIRBE/COBE* and *FIRAS/COBE*) and gas tracers (HI and  $H_\alpha$ ). To study the IR to millimeter properties of the diffuse sky at high galactic latitude, we concentrate on the emission correlated with the HI gas. We compute the emission spectrum of the dust/free-free/synchrotron components associated with HI gas from low to large column densities. A significant residual *WMAP* emission over the free-free, synchrotron and the dust contributions is found from 3.2 to 9.1 mm. We show that this residual *WMAP* emission (normalised to  $10^{20}$  atoms/cm<sup>2</sup>) (1) exhibits a constant spectrum from 3.2 to 9.1 mm and (2) significantly decreases in amplitude when  $N_{\text{HI}}$  increases, contrary to the HI-normalised far-infrared emission which stays rather constant. It is thus very likely that the residual *WMAP* emission is not associated with the Large Grain dust component. The decrease in amplitude with increasing opacity resembles in fact to the decrease of the transiently heated dust grain emission observed in dense interstellar clouds. This is supported by an observed decrease of the HI-normalised 60  $\mu\text{m}$  emission with HI column densities. Although this result should be interpreted with care due to zodiacal residual contamination at 60  $\mu\text{m}$ , it suggests that the *WMAP* excess emission is associated with the small transiently heated dust particles. On the possible models of this so-called “anomalous microwave emission” linked to the small dust particles are the spinning dust and the excess millimeter emission of the small grains, due to the cold temperatures they can reach between two successive impacts with photons.

**Key words.** ISM: general – Cosmology: miscellaneous – Radio continuum: general

## 1. Introduction

At millimeter wavelengths, one of the major challenges in high sensitivity Cosmic Microwave Background (CMB) anisotropy study is to determine the fraction of the observed signal due to diffuse galactic foregrounds. Three different components have been firmly identified at high latitudes ( $|b| > 10^\circ$ ): thermal dust emission, synchrotron and free-free. Dust emission dominates the far-infrared surveys. Its spatial distribution and frequency dependence are quite well-determined for wavelengths shorter than  $\sim 800 \mu\text{m}$ . Above  $\sim 800 \mu\text{m}$ , present data currently do not give any strong constraints. So far, dust emission estimates in the millimeter range are thus an extrapolation of what is known at shorter wavelengths. Synchrotron radiation dominates radio-frequency surveys, but Banday & Wolfendale (1991) and Bennett et

al. (1992) showed that the spectral index steepens with frequency and exhibits spatial variations which are poorly known. Free-free emission has a well-determined spectral behavior and templates are now available thanks to the *WHAM*  $H_\alpha$  survey of the northern sky (Reynolds et al. 1998, Haffner 1999) and the *SHASSA*  $H_\alpha$  survey of the southern sky (Gaustad et al. 2001).

Cross-correlations of CMB data with far-infrared maps have revealed the existence of a microwave emission component (the so-called “anomalous microwave emission”) with spatial distribution traced by these maps. This component has a spectral index suggestive of free-free emission and so has been first interpreted as free-free emission (Kogut et al. 1996). However, Kogut (1999) showed in small parts of the sky that were covered by  $H_\alpha$  data that the microwave emission was consistently brighter than the free-free emission traced by  $H_\alpha$ . Thus, the correlated component cannot be due to free-free emission alone. This is confirmed more recently by Banday et al. (2003) also using *COBE/DMR* data.

Recent works suggest that this anomalous far-infrared correlated component originates from spinning dust grain

Send offprint requests to: Guilaine.Lagache@ias.u-psud.fr

<sup>★</sup> The Wilkinson Microwave Anisotropy Probe (*WMAP*) is the result of a partnership between Princeton University and NASA’s Goddard Space Flight Center

emission (Draine & Lazarian 1998a, De Oliveira-Costa et al. 1999, 2002), tentatively detected at 5, 8 and 10 GHz by Finkbeiner et al. (2002). An alternative explanation is provided by thermal fluctuations in the magnetization of interstellar grains causing magnetic dipole radiation (Draine & Lazarian 1999). However, very recently, Bennett et al. (2003) using *WMAP* data do not find any evidence for the anomalous microwave emission. Their foreground component model comprises only free-free, synchrotron and thermal dust emission, and the observed galactic emission matches the model to  $<1\%$ . Note that in their global analysis, they are dominated by the brightest parts of the sky i.e. the galactic plane and the high latitude dense interstellar clouds. Thus, results may not apply to the most diffuse regions.

We present in this paper a new study of the galactic contributions to the millimeter sky, based on an analysis of the *WMAP* data combined with several templates of dust emission (*DIRBE/COBE* and *FIRAS/COBE*) and gas tracers (HI and  $H_\alpha$ ). We focus only on the high latitude regions where the results are easier to interpret in term of physical properties of dust and where CMB analysis are performed. The paper is organised as follows. We first present the data we use together with their preparation (Sect. 2). We then derive the spectrum (from 100  $\mu\text{m}$  to 10 mm) of the HI-correlated component (Sect 3.1) and show that there exists a residual microwave emission (over free-free, synchrotron and far-infrared dust emission) whose HI-normalised amplitude decreases when the HI column density increases but without any significant spectral variations (Sect. 3.2). We then discuss the results in Sect. 4.

## 2. Data-sets used and their preparation

### 2.1. COBE data

The *COBE* satellite was developed by NASA’s Goddard Space Flight Center to measure the diffuse infrared and microwave radiation from the early universe to the limits set by our astrophysical environment. It was launched November 18, 1989 and carried three instruments:

- a Far Infrared Absolute Spectrophotometer (*FIRAS*) to compare the spectrum of the cosmic microwave background radiation with a precise blackbody (at each sky position, with an angular resolution of  $7^\circ$ , we have one spectrum from 1 to 97  $\text{cm}^{-1}$ )
- a Differential Microwave Radiometer (*DMR*) to map the cosmic radiation (at 31, 53, 90 GHz with a  $7^\circ$  beam)
- a Diffuse Infrared Background Experiment (*DIRBE*) to search for the cosmic infrared background radiation (10 photometric bands from 1 to 240  $\mu\text{m}$  with an angular resolution of  $40'$ ).

*COBE* data are presented in a quadrilateralized spherical projection (the so-called *COBE* Quadrilateralized

Spherical Cube, CSC), an approximately equal-area projection in which the celestial sphere is projected onto an inscribed cube. The *DIRBE* convention is to divide each cube face into  $256 \times 256$  pixels; thus all sky-maps have  $256 \times 256 \times 6 = 393216$  pixels. Each pixel is approximately  $0.32^\circ$  on a side. For *FIRAS* and *DMR*, each cube face is  $32 \times 32$  pixels leading to a total of 6144 pixels (of  $\sim 2.6^\circ$ ).

We use the so-called (i) “Sky Maps and Analyzed Science Data Sets” *DMR* Data (ii) “Galactic Dust Continuum Spectra and Interstellar Dust Parameters” *FIRAS* data, that give the residual sky spectrum after modelled emission from the CMB, zodiacal emission, and interstellar lines have been subtracted. (iii) *DIRBE* “Zodi-Subtracted Mission Average (ZSMA) Maps” for which the zodiacal light intensities were subtracted week by week and the residual intensity values were averaged to create Maps. All *COBE* data are available at <http://lambda.gsfc.nasa.gov/product/cobe>.

### 2.2. Gas tracers

The HI data we used are those of the Leiden/Dwingeloo survey which covers the entire sky down to  $\delta = -30^\circ$  with a grid spacing of  $30'$  in both  $l$  and  $b$ . The  $36'$  half power beam width of the Dwingeloo 25m telescope provides 21 cm maps at an angular resolution which closely matches that of the *DIRBE* maps. Details of the observations and correction procedures are given by Hartmann (1994) and by Hartmann & Burton (1997). It should be noted that in this data-set special care was taken for the removal of far sidelobes emission which makes it particularly suitable for high latitude studies. We derive the HI column densities using  $1 \text{ K km s}^{-1} = 1.82 \cdot 10^{18} \text{ H cm}^{-2}$  (optically thin emission).

Thanks to the *WHAM* survey of the northern sky (Reynolds et al. 1998, Haffner 1999) and the *SHASSA* survey of the southern sky (Gaustad et al. 2001), it is now possible to have a whole sky map of the  $H_\alpha$  emission (Dickinson et al. 2003, Finkbeiner 2003). Since the HI maps cover the sky down to  $\delta = -30^\circ$ , the  $H_\alpha$  emission we use in our analysis is mostly given by the *WHAM* survey. *WHAM* provides a  $12 \text{ km s}^{-1}$  velocity resolution with one-degree angular resolution down to sensitivity limits of  $0.2 \text{ R}$  ( $1 \text{ R} = 10^6 / 4\pi \text{ ph cm}^{-2} \text{ s}^{-1} \text{ sr}^{-1}$ ) in a 30 second exposure. The one-degree angular resolution nicely matches the *DIRBE* resolution. We use the  $H_\alpha$  map and the conversion factors to free-free emission (using  $T_e = 8000 \text{ K}$ ) from Finkbeiner (2003) to derive templates of free-free emission. Since we work only on high latitude regions, the  $H_\alpha$  emission has not been corrected for extinction (the dust absorption is likely to be very small, less than 5%). The free-free templates are used to derive a well-understood contribution to the millimeter channels.

### 2.3. Synchrotron templates

Synchrotron emission arises from relativistic cosmic ray electrons spiralling in the galactic magnetic field. This emission dominates surveys at radio frequencies. The only all-sky map at low frequencies that probe the synchrotron emission is the 408 MHz survey of Haslam et al. (1982). For many years, this map has been used to predict the synchrotron emission in the millimeter channels, assuming a frequency dependence with a constant spectral index of about 2.75. However, Bennett et al. (2003) have shown that the synchrotron spectral index exhibit strong spatial variations and is steeper in the *WMAP* bands than at radio frequencies. We thus use the *WMAP* synchrotron maps derived by Bennett et al. (2003) using the Maximum Entropy Method as frequency dependent well-determined synchrotron templates.

### 2.4. *WMAP* data

The *WMAP*<sup>1</sup> (Wilkinson Microwave Anisotropy Probe) mission, designed to determine the geometry, content, and evolution of the universe, has successfully provided full sky maps at 23, 33, 41, 61 and 94 GHz at respectively 13.2, 39.6, 30.6, 21 and 13.2' FWHM resolution with unprecedented sensitivity. A detailed description of the delivered data-sets for the first 12 months of operation of *WMAP* is given in the *WMAP: explanatory Supplement* (editor M. Limon et al., Greenbelt, MD: NASA/GSFC). The data we use are the first-year “Smoothed I maps” which are the temperature maps at each frequency, smoothed to a common resolution of 1 degree. Data are delivered in the HEALPix<sup>2</sup> format with  $N_{\text{side}}=256$

### 2.5. Data preparation

All the data have to be put in the same projection and at the same resolution. The resolution is set by the *FIRAS* experiment since it is the lowest resolution of our data-sets (7°). All data but *DMR* and *FIRAS* are thus converted in the *DIRBE* CSC format and then convolved with the *FIRAS* beam and degraded to the *FIRAS* CSC resolution (see Lagache 2003 for more details).

We have removed for each data-set the cosecant law variation (1) to avoid the obvious large scale correlations between all galactic components concentrated in the disc and (2) to be consistent with the *WMAP* data that measure only differentially on the sky and thus does not measure the largest angular scales.

We restrict our analysis to  $|b| > 15^\circ$  and exclude the Small and Large Magellanic clouds, together with the  $\rho$  - Ophiucus complex. We also remove cold molecular complexes (as the Taurus cloud), and regions where the dust

is locally heated by nearby stars (like the HII regions) following Lagache et al. (1998). We stress out that this latter pixel selection, although necessary to keep in the analysis only diffuse parts of the sky, does not change the results and conclusions of the paper.

## 3. Analysing the data

### 3.1. Deriving the HI-correlated component spectrum

The HI-correlated dust emission is the dominant component at high galactic latitude at infrared/far-infrared/submillimeter wavelengths (except in the very low HI column density regions where the Cosmic Infrared Background becomes an important contribution, e.g. Lagache et al. 1999). One way to study the infrared to millimeter properties of the diffuse sky at high galactic latitude is therefore to concentrate on the emission correlated with the HI gas. We search here for the spatial/spectral variations of the infrared to millimeter emission with the HI gas column densities.

To compute the emission spectrum of the component associated with HI gas from low to large column densities, we use a differential method that removes, within statistical variance, any residual infrared emission that is not correlated with the HI gas such as an isotropic component. We first select sky pixels according to their HI column density and sort them into sets of pixels bracketed by selected values of  $N_{\text{HI}}$ . Correlated HI emission spectra are then computed for each set of pixel  $k$  using the equation:

$$F_\nu(k) = \frac{\langle F \rangle_k - \langle F \rangle_0}{\langle N_{\text{HI}} \rangle_k - \langle N_{\text{HI}} \rangle_0} \quad (1)$$

where  $\langle F \rangle_i$  corresponds to the mean emission computed for the set of pixels  $i$ , and  $\langle N_{\text{HI}} \rangle_i$  to the mean HI column density for the same set of pixels. Note that all the data-sets used here are cosecant-law subtracted (see Sect. 2.5).

To keep high signal-to-noise ratio, only 5 sets of pixels are considered here, with increasing  $N_{\text{HI}}$ . The first set (labeled “0” in Eq. (1)), serves as the “reference” set and corresponds to the lowest column density regions (representing  $\sim 5\%$  of the sky). We are thus left with 4 sets of pixels  $k$  with increasing  $N_{\text{HI}}$  and derive accordingly four mean spectra  $F_\nu(k)$ . The sets of pixels are selected on the cosecant-law removed HI emission that can be negative. For reference, the total mean HI column density (i.e. non cosecant-law subtracted) for the 4 bins are 3.3, 4.1, 5.6 and 9.9  $10^{20}$  at/cm<sup>2</sup>. By construction, the spectra are normalised to  $10^{20}$  at/cm<sup>2</sup>. Note that  $F$  in Eq. (1) represents alternatively the *DIRBE*, *FIRAS*, *DMR*, *WMAP*, free-free and synchrotron data.

<sup>1</sup> <http://lambda.gsfc.nasa.gov/product/map/>

<sup>2</sup> <http://www.eso.org/science/healpix>

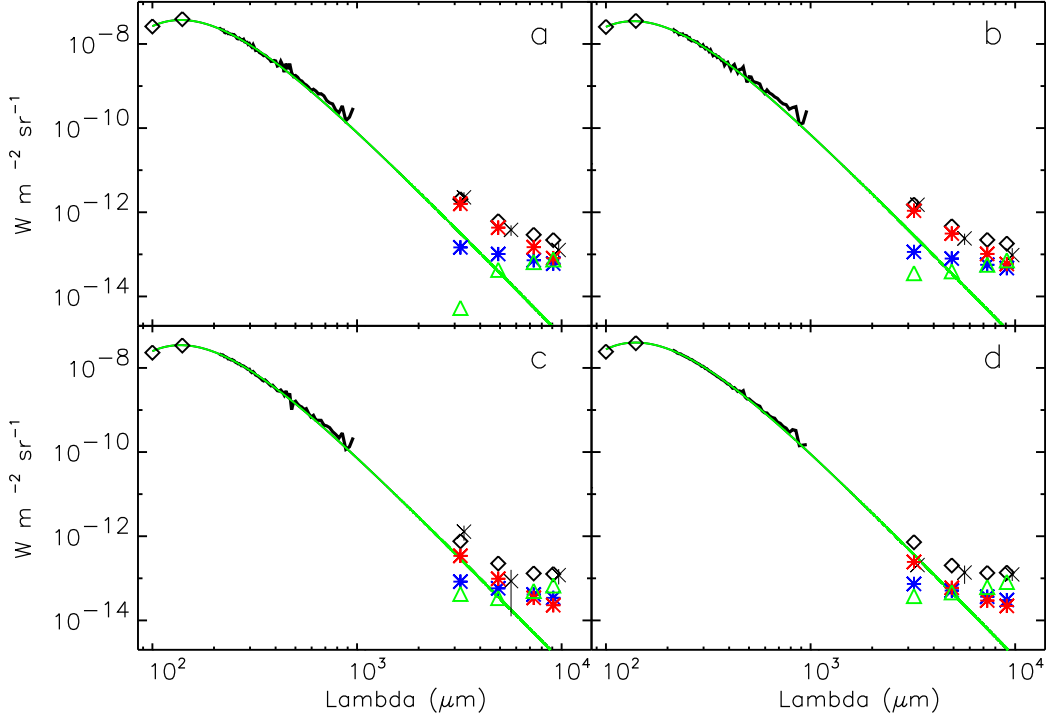


**Fig. 1.** Spectrum of the HI-correlated component normalised to  $10^{20}$  at/cm $^2$  (with increasing N(HI) from a to d). The black diamonds at 100 and 140  $\mu$ m are the *DIRBE* data, the black curve is the *FIRAS* spectrum, the black crosses with error bars are the *DMR* data and the black triangles at 3.2, 4.9, 7.3 and 9.1 mm are the *WMAP* data. Also displayed are the free-free and synchrotron contributions (blue stars and green triangles respectively). The green continuous line is the result of a fit of the *DIRBE* 100, 140  $\mu$ m and *FIRAS* spectra ( $200 < \lambda < 500$   $\mu$ m) with a modified Planck curve with a  $\nu^2$  emissivity law (the so-called stable thermal dust component). The residual *WMAP* emission (which is the *WMAP*- free-free - synchrotron - stable thermal dust component) is shown as red stars.

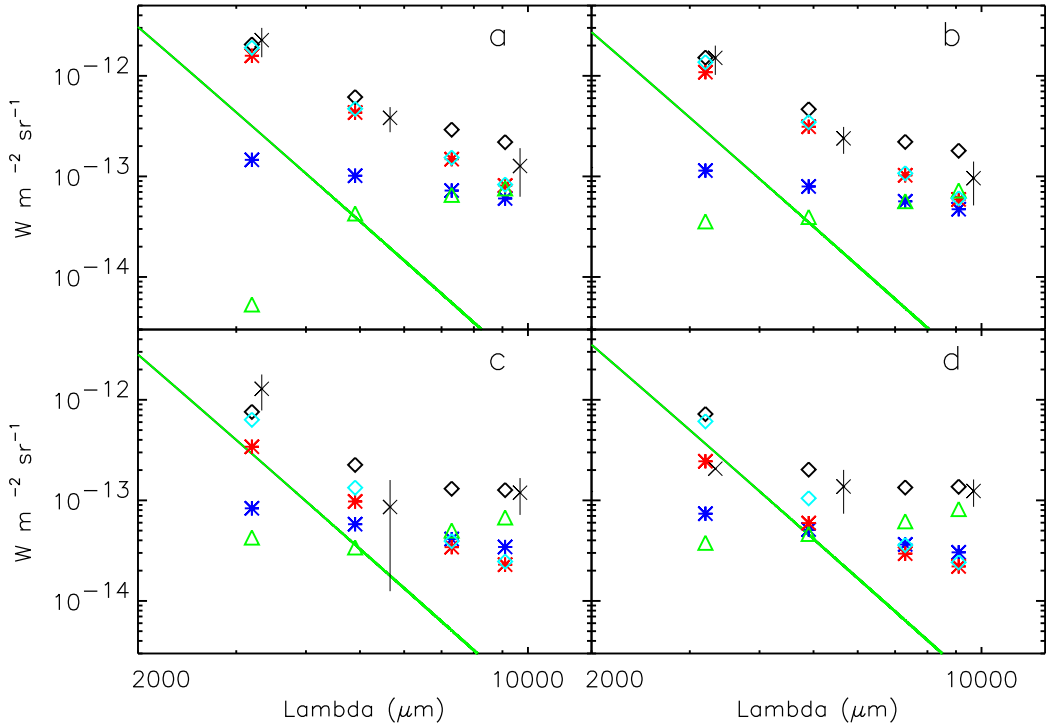


**Fig. 2.** Zoom on the millimeter part of Fig. 1. Symbols and colors are the same as on Fig. 1. Added is the residual *WMAP* emission after having removed only the free-free and synchrotron contributions (light-blue diamonds).

Component		3.2 mm	4.3 mm	7.9 mm	9.1 mm
<i>WMAP</i>	1	$2.05 \cdot 10^{-12}$	$6.15 \cdot 10^{-13}$	$2.92 \cdot 10^{-13}$	$2.19 \cdot 10^{-13}$
	2	$1.52 \cdot 10^{-12}$	$4.65 \cdot 10^{-13}$	$2.25 \cdot 10^{-13}$	$1.80 \cdot 10^{-13}$
	3	$7.59 \cdot 10^{-13}$	$2.26 \cdot 10^{-13}$	$1.31 \cdot 10^{-13}$	$1.27 \cdot 10^{-13}$
	4	$7.22 \cdot 10^{-13}$	$2.03 \cdot 10^{-13}$	$1.34 \cdot 10^{-13}$	$1.37 \cdot 10^{-13}$
<i>Free-free</i>	1	$1.46 \cdot 10^{-13}$	$1.02 \cdot 10^{-13}$	$7.23 \cdot 10^{-14}$	$6.03 \cdot 10^{-14}$
	2	$1.14 \cdot 10^{-13}$	$7.93 \cdot 10^{-14}$	$5.65 \cdot 10^{-14}$	$4.71 \cdot 10^{-14}$
	3	$8.33 \cdot 10^{-14}$	$5.79 \cdot 10^{-14}$	$4.12 \cdot 10^{-14}$	$3.44 \cdot 10^{-14}$
	4	$7.36 \cdot 10^{-14}$	$5.12 \cdot 10^{-14}$	$3.64 \cdot 10^{-14}$	$3.04 \cdot 10^{-14}$
<i>Synchrotron</i>	1	$5.32 \cdot 10^{-15}$	$4.28 \cdot 10^{-14}$	$6.56 \cdot 10^{-14}$	$7.60 \cdot 10^{-14}$
	2	$3.57 \cdot 10^{-14}$	$3.95 \cdot 10^{-14}$	$5.67 \cdot 10^{-14}$	$7.24 \cdot 10^{-14}$
	3	$4.27 \cdot 10^{-14}$	$3.40 \cdot 10^{-14}$	$5.01 \cdot 10^{-14}$	$6.76 \cdot 10^{-14}$
	4	$3.79 \cdot 10^{-14}$	$4.64 \cdot 10^{-14}$	$6.19 \cdot 10^{-14}$	$8.20 \cdot 10^{-14}$
<i>Stable thermal dust</i>	1	$3.17 \cdot 10^{-13}$	$3.95 \cdot 10^{-14}$	$5.53 \cdot 10^{-15}$	$1.86 \cdot 10^{-15}$
	2	$2.81 \cdot 10^{-13}$	$3.50 \cdot 10^{-14}$	$4.90 \cdot 10^{-15}$	$1.64 \cdot 10^{-15}$
	3	$2.91 \cdot 10^{-13}$	$3.62 \cdot 10^{-14}$	$5.08 \cdot 10^{-15}$	$1.71 \cdot 10^{-15}$
	4	$3.66 \cdot 10^{-13}$	$4.55 \cdot 10^{-14}$	$6.39 \cdot 10^{-15}$	$2.15 \cdot 10^{-15}$
<i>Residue</i>	1	$1.58 \cdot 10^{-12}$	$4.31 \cdot 10^{-13}$	$1.48 \cdot 10^{-13}$	$8.11 \cdot 10^{-14}$
	2	$1.09 \cdot 10^{-12}$	$3.12 \cdot 10^{-13}$	$1.02 \cdot 10^{-13}$	$5.89 \cdot 10^{-14}$
	3	$3.41 \cdot 10^{-13}$	$9.75 \cdot 10^{-14}$	$3.42 \cdot 10^{-14}$	$2.29 \cdot 10^{-14}$
	4	$2.45 \cdot 10^{-13}$	$5.94 \cdot 10^{-14}$	$2.95 \cdot 10^{-14}$	$2.20 \cdot 10^{-14}$

**Table 1.** *WMAP*, free-free, synchrotron and stable thermal dust component emission (in  $\text{W}/\text{m}^2/\text{sr}$ , normalised to  $10^{20} \text{ at}/\text{cm}^2$ ) in the four HI bins together with the residual emission (which is equal to *WMAP* - Free-free - Synchrotron - Stable thermal dust). The mean total HI column densities are 3.3, 4.1, 5.6 and  $9.9 \cdot 10^{20} \text{ at}/\text{cm}^2$  for the bin 1, 2, 3 and 4 respectively.

### 3.2. Results

The four spectra are presented on Fig. 1 with the *DIRBE* data points at 100 and  $140 \mu\text{m}$ , the *FIRAS* spectra (displayed only between 210 and  $1000 \mu\text{m}$ ), the *DMR* data points at 90, 53 and 31 GHz and the *WMAP* data points at 3.2, 4.9, 7.3 and 9.1 mm (all these data points are in black on Fig. 1). A zoom on the millimeter part of the figure is presented on Fig. 2. We fit the *DIRBE* 100,  $140 \mu\text{m}$  and *FIRAS* spectra ( $200 < \lambda < 500 \mu\text{m}$ ) with a modified Planck curve with a  $\nu^2$  emissivity law (the result of the fit is displayed on Fig. 1 and 2). We know that this fit is inconsistent with *FIRAS* data below  $\sim 500 \text{ GHz}$  where an excess component is detected (Reach et al. 1995, Finkbeiner et al. 1999). However, discussing this component is not the goal of this paper. We only concentrate on the millimeter part on the spectra and how it relates to the far-infrared emission. It is important to note that this far-infrared dust emission has a stable spectrum, not changing with increasing opacity (Lagache et al. 1999). In this framework, the  $\nu^2$  modified black body is well representative and useful for comparison between spectral far-infrared and millimeter shapes<sup>3</sup>. This far-infrared dust emission extrapolated at millimeter wavelengths will be called the “stable thermal dust component”.

First, we see on Fig. 2 that there is a strong millimeter excess (with both *DMR* and *WMAP* data) with respect

to the stable thermal dust component (i.e the  $\nu^2$  modified black body). This excess decreases significantly (by a factor of about 5 at 3.2 mm) when the HI column density increases, although the far-infrared emission remains nearly constant (at the  $\sim 6\%$  level). The far-infrared emission is dominated by the so-called Large Grain dust component. The millimeter excess, which changes rapidly with opacity, is thus not likely associated with this dust component.

We can go further by removing to the *WMAP* emission the corresponding free-free, synchrotron and stable thermal dust component contribution. The residual *WMAP* emission is shown on Fig. 1 and 2 (red stars) and detailed in Table 1. First, at each frequency, the residual emission exhibits a strong decrease (by about a factor of 5) with HI column densities (from bin 1 to 4). Second, the residual emission decreases from 3.2 to 9.1 mm in each HI bin. On Fig. 3 are shown the *WMAP* residual emissions for the 4 bins at 3.2, 4.9, 7.3 and 9.1 mm, normalised to the 90 GHz *DMR* residual emission (the 31 and 53 GHz *DMR* residual emissions have also been computed but are not displayed to avoid confusion. Results, although more noisy, are in very good agreement with *WMAP*). This figure shows that we do not detect any significant variations in the spectral shape of the residual emission<sup>4</sup>. Thus, the HI-normalised residual emission, although decreasing in amplitude with the HI column density, has a constant spectrum.

<sup>3</sup> The way we are fitting the far-infrared stable component is not critical since we focus on the variable millimeter emission.

<sup>4</sup> This however will have to be quantified when smoothed *WMAP* data with error bars will be available.

	HI bin 1	HI bin 2	HI bin 3	HI bin 4
$\nu R_\nu(3.2 \text{ mm})$	$1.58 \cdot 10^{-12}$	$1.09 \cdot 10^{-12}$	$3.41 \cdot 10^{-13}$	$2.45 \cdot 10^{-13}$
$\nu R_\nu(4.9 \text{ mm})$	$4.31 \cdot 10^{-13}$	$3.12 \cdot 10^{-13}$	$9.75 \cdot 10^{-14}$	$5.94 \cdot 10^{-14}$
$\nu R_\nu(7.3 \text{ mm})$	$1.48 \cdot 10^{-13}$	$1.02 \cdot 10^{-13}$	$3.42 \cdot 10^{-14}$	$2.95 \cdot 10^{-14}$
$\nu R_\nu(9.1 \text{ mm})$	$8.11 \cdot 10^{-14}$	$5.89 \cdot 10^{-14}$	$2.29 \cdot 10^{-14}$	$2.20 \cdot 10^{-14}$
$\nu I_\nu(240 \text{ } \mu\text{m})$	$1.81 \cdot 10^{-8}$	$1.63 \cdot 10^{-8}$	$1.59 \cdot 10^{-8}$	$1.83 \cdot 10^{-8}$
$\nu I_\nu(140 \text{ } \mu\text{m})$	$3.90 \cdot 10^{-8}$	$3.54 \cdot 10^{-8}$	$3.41 \cdot 10^{-8}$	$3.90 \cdot 10^{-8}$
$\nu I_\nu(100 \text{ } \mu\text{m})$	$2.61 \cdot 10^{-8}$	$2.54 \cdot 10^{-8}$	$2.31 \cdot 10^{-8}$	$2.43 \cdot 10^{-8}$
$\nu I_\nu(60 \text{ } \mu\text{m}) \text{ }  \beta  > 3^\circ$	$1.16 \cdot 10^{-8}$	$9.37 \cdot 10^{-9}$	$7.18 \cdot 10^{-9}$	$6.48 \cdot 10^{-9}$
$\nu I_{\nu\text{VSG}}(60 \text{ } \mu\text{m}) \text{ }  \beta  > 3^\circ$	$9.24 \cdot 10^{-9}$	$6.98 \cdot 10^{-9}$	$4.94 \cdot 10^{-9}$	$4.21 \cdot 10^{-9}$
$\nu I_\nu(60 \text{ } \mu\text{m}) \text{ }  \beta  > 15^\circ$	$9.34 \cdot 10^{-9}$	$7.23 \cdot 10^{-9}$	$4.57 \cdot 10^{-9}$	$4.92 \cdot 10^{-9}$
$\nu I_{\nu\text{VSG}}(60 \text{ } \mu\text{m}) \text{ }  \beta  > 15^\circ$	$7.01 \cdot 10^{-9}$	$4.83 \cdot 10^{-9}$	$2.32 \cdot 10^{-9}$	$2.65 \cdot 10^{-9}$

**Table 2.** Excess residual emission ( $\nu R_\nu$ ) at 3.2, 4.9, 7.3 and 9.1 mm with 240, 140, 100 associated brightnesses (in  $\text{W/m}^2/\text{sr}$ , normalised to  $10^{20} \text{ at/cm}^2$ ) for the 4 HI bins. The  $60 \text{ } \mu\text{m}$  brightness is given for  $|\beta| > 3^\circ$  and  $|\beta| > 15^\circ$  to show that the decrease may not be due to any residual zodiacal light emission. Also given are the  $60 \text{ } \mu\text{m}$  brightnesses corresponding to the Very Small Grains dust component only (we have removed from the  $60 \text{ } \mu\text{m}$  emission,  $I(60 \text{ } \mu\text{m})$ , the best  $\nu^2$  modified black body fit done on the Large Grain dust component).

#### 4. Discussion

To account for the galactic energy emitted from the mid-infrared to the submillimeter, it is necessary to have a broad dust size distribution from large grains down to large molecules. For example, Désert et al. (1990) (see also Draine & Anderson 1985, Puget et al. 1995, Weiland et al. 1986, Siebenmorgen & Krügel 1992, Dwek et al. 1997 and more recently Li & Draine 2001) have proposed a consistent interpretation of both the infrared emission in diffuse HI clouds and the interstellar extinction curve using a model with three components: PAHs (Polycyclic Aromatic Hydrocarbons), Very Small Grains (VSGs) and Large Grains. PAHs and VSGs are small enough ( $a \leq 10 \text{ nm}$ ) to experience significant temperature fluctuations after photon absorption. They emit over a wide range of temperatures and dominate the emission for  $\lambda \leq 60 \text{ } \mu\text{m}$ . The Large Grain component is the more traditional dust component historically inferred from optical studies. These grains are in equilibrium with the incident radiation field with a temperature of about 17 K in the diffuse atomic medium (Boulanger et al. 1996). The Large Grain dust component is expected, at long wavelengths, to be proportional to the total amount of solid material. The large spatial variations of the infrared spectrum over the wavelengths range 12–60  $\mu\text{m}$  have been interpreted as changes in the abundance of small grains (Boulanger et al. 1990, Laureijs et al. 1991, Bernard et al. 1993, Abergel et al. 1994). In particular, strong deficits of the transiently heated grains emitted at  $60 \text{ } \mu\text{m}$  are observed in dense interstellar clouds, these deficits being explained by grain-grain coagulation processes (e.g. Stepnik et al. 2003).

It has been shown in Sect 3.2 that the HI-normalised residual *WMAP* emission (i.e. the excess above free-free and synchrotron contributions and the stable thermal dust component) is well traced at large scale by the

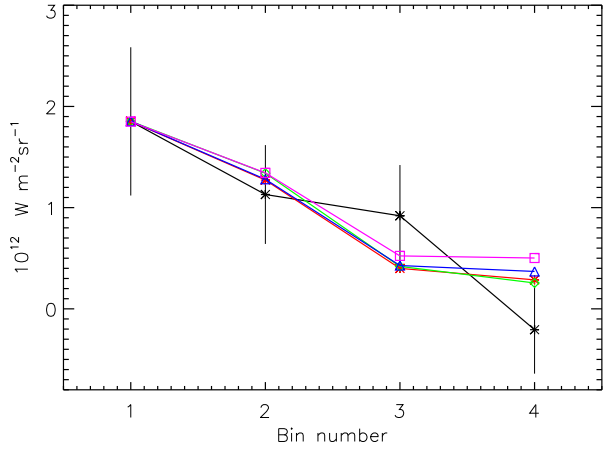


**Fig. 3.** HI-normalised residual *WMAP* emission at 3.2 (red), 4.9 (green), 7.3 (blue) and 9.1 (magenta) mm. All spectra are normalised on the *DMR* 90 GHz residual emission for the first HI bin (black points with error bars). The HI column density increases from bin 1 to 4 (from  $3.3$  to  $9.9 \cdot 10^{20} \text{ at/cm}^2$ ). No significant variations in the spectral shape of the residual emission is detected.

HI gas and (1) exhibits a constant spectrum from 3.2 to 9.1 mm but (2) significantly decreases in amplitude when  $N_{\text{HI}}$  increases, contrary to the far-infrared emission (associated with the so-called stable thermal dust component) which stays rather constant (cf. Table 2). It is thus very likely that the residual *WMAP* emission is not associated with the Large Grain dust component. The decrease in amplitude resembles in fact to the decrease of the PAH/VSGs emission observed in dense interstellar clouds. By extrapolating the PAH/VSGs behaviour from dense interstellar clouds to the diffuse medium, we may expect, when increasing the HI column density, to

decrease the PAH and VSGs proportion and thus the mid-infrared emission. If this is true, then the PAH/VSGs HI-correlated emission should decrease with HI column densities. This decrease, if present, is very hard to observe in the mid-infrared due to the strong residual interplanetary dust emission at large scale. On the *DIRBE* bands, only the 60  $\mu\text{m}$  may be used. We have computed for the 4 HI bins the 60  $\mu\text{m}$  HI-correlated emission with two different cuts in ecliptic latitude ( $|\beta| > 3^\circ$  and  $|\beta| > 15^\circ$ ). Although the absolute level of the 60  $\mu\text{m}$  HI-correlated emission varies for the 2 cuts, we observe nearly the same significant decrease of the 60  $\mu\text{m}$  emission with the HI column density (cf. Table 2). The 60  $\mu\text{m}$  band may be contaminated by the Large Grain emission (30 to 40 %, e.g. Désert et al. 1990). Therefore, we remove to the 60  $\mu\text{m}$  emission the Large Grain contamination using the best  $\nu^2$  modified black body fit (Fig. 1). The observed decrease at 60  $\mu\text{m}$  becomes even larger (Table 2). Although this result should be interpreted with care due to the zodiacal contamination at 60  $\mu\text{m}$ , it suggests that the *WMAP* residual emission is associated with the small transiently heated particles.

The previous results suggest the anomalous microwave component is associated with the transiently heated dust particles, but its exact physical mechanism remains to be found. On the possible models of the anomalous emission linked to the transiently heated particles are:

- The “spinning-dust” which is the rotational emission from very small dust grains (Draine & Lazarian, 1998a, 1998b). However, although the spinning dust emission is in good agreement with the *WMAP* emission at 7.3 and 9.1 mm, it is inconsistent with the 3.2 mm emission.
- The VSGs long-wavelength emission. VSGs are transiently heated when an ultraviolet photon is absorbed. The mean interval between successive ultraviolet photons is longer than the cooling time and thus, between 2 impacts, the temperature of the particles is very low (but is at least the CMB temperature). Such particles could therefore emit significant emission in the millimeter channels.

The models have large uncertainties linked to the unknown properties of the small particles. It is therefore very difficult to predict the exact contribution of the two in the millimeter.

*Acknowledgements.* The author thanks the *WMAP* team for having provided to the community beautiful data. Many thanks to J.-L. Puget and F. Boulanger for having carefully read this paper and for fruitful discussions. Thanks also to J.-P. Bernard for his help in the data manipulation.

## References

Abergel A., Boulanger F., Mizuno A. & Fukui Y., 1994, *ApJ* 423, L59  
 Banday A.J. & Wolfendale A.W., 1991, *MNRAS* 248, 705

Banday A.J., Dickinson C., Davies R.D. et al., 2003, *MNRAS* submitted  
 Bernard J.P., Boulanger F. & Puget J.-L., 1993, *ApJ* 277, 609  
 Bennett C.L., Smoot G.F. & Hinshaw G., 1992, 396, L7  
 Bennett C.L., Hill R.S., Hinshaw G. et al., 2003, *ApJ*, submitted  
 Boulanger F., Abergel A., Bernard J.-P. et al. 1996, *A&A* 312, 256  
 Boulanger F., Falgarone E., Puget J.-L. & Helou G., 1990, *ApJ* 364, 136  
 Désert F.-X., Boulanger F., Puget J.-L., 1990, *A&A* 327, 215  
 De Oliveira-Costa A., Tegmark M., Gutierrez C. et al., 1999, *ApJ* 527, L9  
 De Oliveira-Costa A., Tegmark M., Finkbeiner D., et al., 2002, *ApJ* 567, 363  
 Dickinson C., Davies R.D. & Davis R.J., 2003, *MNRAS*, in press  
 Draine B.T. & Anderson N. 1985, *ApJ* 292, 494  
 Draine B.T. & Lazarian A., 1998a, *ApJ* 494, L19  
 Draine B.T. & Lazarian A., 1998b, *ApJ* 508, 157  
 Draine B.T. & Lazarian A., 1999, *ApJ* 512, 740  
 Dwek E., Arendt, R.G., Fixsen, D.J. et al. 1997, *ApJ* 475, 565  
 Finkbeiner D., Davis M. & Schlegel D.J., 1999, *ApJ* 524, 867  
 Finkbeiner D., Schlegel D.J., Frank C. & Heiles C., 2002, *ApJ* 566, 898  
 Finkbeiner D., 2003, *ApJS*, in press  
 Gaustad J.E., Mc Cullough P.R., Rosing W.R. & Buren D.V., 2001, *PASP* 113, 1326  
 Haffner L.M., 1999, Ph.D. Thesis, University of Wisconsin  
 Hartmann D., 1994, Ph.D. Thesis, University of Leiden  
 Hartmann D. & Burton W.B., Cambridge University Press, 1997  
 Haslam C.G.T., Salter C.J., Stoffel H. & Wilson W., 1982, *A&AS* 47, 1  
 Kogut A., Banday A.J., Bennett C.L. et al., 1996, *ApJ* 460, 1  
 Kogut A., 1999, in *ASP Conf. Ser.* 181, *Microwave Foregrounds*, ed. A. De Oliveira Costa & M. Tegmark, in press  
 Lagache G., Abergel A., Boulanger F. & Puget J.-L., 1998, *A&A* 333, 709  
 Lagache G., Abergel A., Boulanger F., et al., 1999, *A&A* 344, 322  
 Lagache G., 2003, “Absolute photometric calibration of *Planck/HFI* high-frequency channels on the Galaxy: Application to Archeops data”, *A&A*, to be submitted  
 Laurejis R.J., Clark F.O. & Prusti T., 1991, *ApJ* 372, 185  
 Li A. & Draine, B.T., 2001, *ApJ* 554, 778  
 Puget, J.L., Léger, A. & Boulanger, F. 1985, *A&A* 142, L19  
 Reach W.T., Dwek E., Fixsen D.J., et al. 1995, *ApJ* 451, 188  
 Reynolds R.J., Tufte S.L., Haffner L.M., et al., 1998, *PASA* 15, 14  
 Siebenmorgen R. & Krügel, E. 1992, *A&A* 259, 614  
 Stepnik B., Abergel A., Bernard J.-P. et al., 2003, *A&A* 398, 551  
 Weiland J.L., Blitz L., Dwek E. et al. 1986, *ApJ* 306, L101